Robust Sparse Unmixing for Hyperspectral Imagery

Dan Wang, Zhenwei Shi, Xinrui Cui

Abstract

Linear sparse unmixing method based on spectral library has been widely used to tackle the hyperspectral unmixing problem, under the assumption that the spectrum of each pixel in the hyperspectral scene can be expressed as a linear combination of pure endmembers in the spectral library. However, because of the ion (atom) substitution in the geological process, there often exists spectral variability between the measured endmembers in the real environment and corresponding ones in the spectral library, which poses a significant challenge to linear sparse unmixing. Physically, the substitution leads to the variation of absorption peaks of endmembers, making the spectral variation of sparse property. To address the above problem, we introduce *redundant spectrum* to represent the spectral variation caused by ion (atom) substitution and develop *Sparse Redundant Unmixing Model* by adding the redundant regularization into the classical sparse regression formulation. Based on the alternating direction method of multipliers (ADMM), we develop a unified algorithm called *Sparse Redundant Unmixing* (SpaRedU) to obtain the solution. Both simulation experiment and real data experiment demonstrate that the proposed method can effectively use the redundant spectrum to address the spectral variation problem caused by the ion (atom) substitution.

Index Terms

Hyperspectral data, library-based linear sparse unmixing, substitution, redundant spectrum.

I. INTRODUCTION

Hyperspectral remote sensing focus on the measurement and analysis of spectra covering a range from the visible to the infrared [1, 2]. Nowadays, it has been widely used in various application fields including food safety, quality control, and risk response, etc [3, 4]. However, due to the insufficient spatial resolution of the hyperspectral imaging spectrometer, multi-scattering, as well as homogenous mixture of different substances, almost each pixel

Dan Wang and Zhenwei Shi (Corresponding Author) is with Image Processing Center, School of Astronautics, Beihang University, Beijing 100191, PR China, with State Key Laboratory of Virtual Reality Technology and Systems, Beihang University, Beijing 100191, PR China and also with Beijing Key Laboratory of Digital Media, Beihang University, Beijing 100191, PR China (e-mail:Dan.Wang@buaa.edu.cn; shizhenwei@buaa.edu.cn).

Xinrui Cui is with the Department of Electrical and Computer Engineering, University of British Columbia, Vancouver, BC V6T 1Z4, Canada (e-mail: wdydcxr@gmail.com).

in the hyperspectral scene contains more than one pure substance [5]. To obtain accurate estimation of substances, unmixing aims at decomposing the spectrum of each mixed pixel into a combination of pure endmembers [6, 7] and a set of corresponding fractional abundances which indicate the proportion of each endmember present in the mixed pixel [8].

Given the mixing scale in each pixel and the geometry in the scene, the observed mixture is either linear [9] or nonlinear [10–12]. In recent years, the linear unmixing model has been well developed because of its advantages like ease of implementation and flexibility [13]. It expresses the measured hyperspectral data of each mixed pixel as a linear combination of endmembers weighted by fractional abundances. In general, the linear unmixing algorithm can be classified as semisupervised algorithm and unsupervised one depending on whether using the spectral library or not. During the past decade, tremendous effort has been put into the unsupervised linear unmixing algorithm. Several unsupervised approaches based on statistics [14, 15], nonnegative matrix factorization (NMF) [16, 17] and geometry [18] have been developed under the linear unmixing model. However, since these approaches extract endmembers merely from the given hyperspectral data, they either may obtain virtual endmembers with no physical meaning [19] or assume the presence of at least one pure pixel per endmember in the data that is often difficult to guarantee [20].

As more expanded spectral libraries become openly available, a semisupervised approach called sparse unmixing [21–23] has been developed, which does not have the problem about virtual endmembers and the assumption of pure pixels. Sparse unmixing aims at using only a few endmembers in a given spectral library to model each mixed pixel in the hyperspectral scene. Since the number of actual endmembers in a hyperspectral scene is usually much smaller than that of endmembers in the library, this approach often leads to a sparse solution. Based on the increasingly mature linear sparse representation techniques [24–27], several effective linear sparse unmixing algorithms have been proposed, such as the sparse unmixing via variable splitting and augmented Lagrangian (SUnSAL) [28], sparse unmixing via variable splitting augmented Lagrangian and total variation (SUnSAL-TV) [29] and the subspace matching pursuit (SMP) [30], and so on.

A drawback of the current sparse unmixing methods is that an actual spectral signature (endmember) in the scene is often assumed to be the same with its corresponding sample in the spectral library, and this assumption is too ideal in the real environment. Spectral variation can result in rather damaging effects on the traditional sparse unmixing methods. Recently, several papers referring to spectral variation have been published. A dictionary-adjusted non-convex sparsity-encouraging regression framework (DANSER) was proposed to address the spectral mismatch problem in hyperspectral unmixing [32]. A model named perturbed linear mixing model was put forward to measure the spectral variability between endmembers in multi-temporal hyperspectral images [33]. Also, Tikhonov regularization was used within the total least squares (TLS) estimation framework to obtain more accurate estimation in hyperspectral unmixing [34].

To the best of our knowledge, little attention has been paid to study spectral variation from its physical mechanism. In practice, one of the most important reason for spectral variation is ion (atom) substitution [31]. With the change of physical and chemical conditions in the geological process, ion (atom) substitution is continuous in minerals

[35]. In this paper, we analyze the physical mechanism of spectral variation caused by ion (atom) substitution. Through the analysis, the sparse property of spectral variation is deduced. Here, we define the spectral variation as *redundant spectrum*. Based on its sparse property, we propose a *sparse redundant unmixing model* that incorporates redundant spectrum as regularization to tackle the above problem. Based on the alternating direction method of multipliers (ADMM) [37, 38], we develop *Sparse Redundant Unmixing* (SpaRedU) algorithm to solve the sparse redundant unmixing model.

The rest of this paper is structured as follows. In Section II, we elaborate the spectral variation problem caused by ion (atom) substitution and explain the reason why the redundant spectrum is sparse. In Section III, a sparse redundant unmixing model is presented and a unified SpaRedU algorithm is proposed to solve the sparse unmixing problem. Section IV illustrates the performance of SpaRedU algorithm with the simulation experiment results. Section V provides an experimental validation of SpaRedU using real hyperspectral data set. Finally, the conclusion is drawn in Section VI.

II. REDUNDANT SPECTRUM

In this section, we elaborate the spectral variation problem caused by ion (atom) substitution. Since ion (atom) substitution is one of the most important reason for spectral variation, here we detailed analyze the physical mechanism of how the substitution results in spectral variation. Based on the analysis, we explain the reason why the spectral variation is sparse.

A. Spectral variation caused by element substitution

In the geological process, actual endmembers measured in the real environment are different from corresponding pure endmembers in the spectral library. Pure endmembers in the spectral library are measured under certain environment conditions. The composition and structure of each pure endmember in the spectral library are constant [39]. In contrast, during the geological process, the compositions and structures of actual endmembers in the real environment usually change slightly and continuously because of ion (atom) substitution. Concretely, under suitable condition of temperature, pressure and pH value, some ions (atoms) in the crystal structure of minerals could be substituted by other ions (atoms) of similar characteristics such as chemical property, radius, and valence state [35]. Here, original ions (atoms) in crystal structure and substitutional ions (atoms) are regarded as hosts and guests, respectively. Take Tremolite for example, Fe^{2+} (guests) can partially substitute for Mg^{2+} (hosts) under proper conditions (shown in Fig. 1).

For a rough mineral identification, one can hold that mineral after ion (atom) substitution can be identified as the same one in spectral library for the following reasons: Firstly, in the geological process, the amount of such substitution is relatively small. Besides, the chemical bond and the charge balance of ions nearly keep invariant after the substitution, whereas only crystalline structure and physical properties (like refractive index, density, etc.) change linearly with the amount of substitution [40].
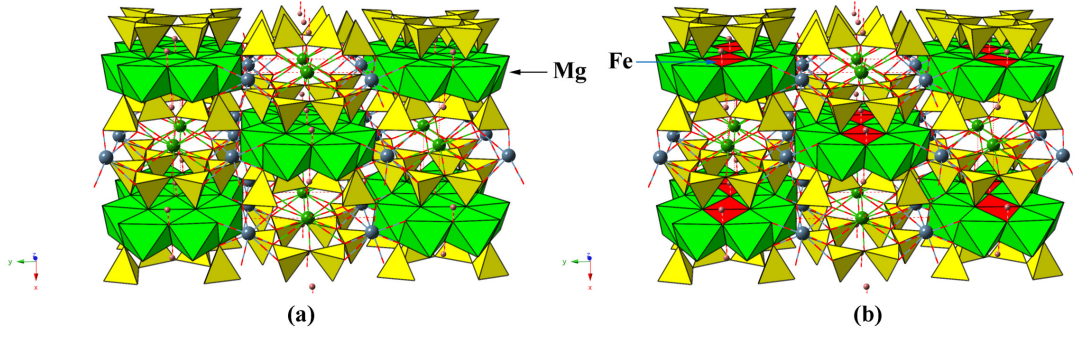
Fig. 1. Crystal structure of Tremolite. (a) original Tremolite, (b) Tremolite after the substitution of Fe^{2+} for Mg^{2+}.

However, since spectrum is sensitive to the variation of crystalline structure, ion (atom) substitution could result in the spectral variation compared with those in the spectral library [41]. Concretely, the substitution can influence the absorption peaks, which are main characteristics of spectra, and result in a sparse spectral variation. The positions of these changed absorption peaks are generally determined by the type of original and substitutional ions (atoms), and the intensity variations of these peaks are influenced by the amount of substitution. The spectral mismatch caused by ion (atom) substitution could bring negative influence on linear sparse unmixing.

B. Mechanism of spectral variation

Here, we provide detailed analysis about the physical mechanism of spectral variation caused by ion (atom) substitution.

In view of a spectrum, the main characteristic is its absorption peaks. Physically, the absorption peaks of endmembers are usually caused by two processes, i.e. electronic and vibrational [43, 44]. According to theoretical calculation, the absorption peaks caused by electronic process locate in near-, mid-infrared region, while the absorption peaks caused by vibrational process appear in visible region. This is because the energy level difference in the vibrational process is relatively smaller than that in the electronic process. For hyperspectral remote sensing, the absorption peaks in $0.4-1.3\mu m$ wavelength region mainly rely on the electronic transition of transition elements (Ni, Fe, Co, etc.), while the absorption peaks in $1.3-2.5\mu m$ are determined by the vibration of radicals (CO_3^{2-}, NH_4^+, etc.) that is sensitive to crystalline structure changes. Accordingly, for endmembers after substitution, the reason of spectral variation includes two aspects, i.e. electronic and vibrational.

In the electronic process, ion (atom) substitution can influence both crystal field effect and charge transfer which play important roles in the appearance of absorption peaks in visible wavelength region. Specifically, ion (atom) substitution alters the arrangement of elements in crystalline structure, changing its crystal field accordingly. For crystal field effect, ions of the transition elements (e.g., Ni, Cr, Fe, etc.) can be greatly influenced by interaction with different crystal fields, resulting in the change in their energy levels [42]. Theoretically, absorption or emission of specific wavelengths of electromagnetic radiation (denoted as photons) takes place as changes between energy

levels occur. Thus, the variation of energy level leads to the absorption of proper photons whose energy match the altered energy difference between energy levels [43]. Charge transfer refers to the process whereby absorbed energy causes an electron to migrate between neighboring ions [42]. The substitution can change the binding force to electrons so that valence electrons need to absorb photons with a different energy to migrate between ions [45]. For both crystal field effects and charge transfer, ion (atom) substitution can cause the variation of the photon absorption, thus making the absorption peaks change.

In the vibrational process, ion (atom) substitution can shift the number and form of normal vibration[1] by changing the number and type of constituent elements and their spatial geometry. Each normal vibration has a frequency associated with it. Normally, an overtone occurs when a normal vibration is excited with two or more quanta of energy, producing a band at twice of the fundamental frequency. A combination tone occurs when two or more different fundamentals or overtones occur, bringing a band located at the sum of all the fundamental or overtone frequencies [42]. Overtones and combinations can be observed in the near-infrared region, while normal vibration of all geologically important minerals fall in mid- and far-infrared regions. Concretely, in near-infrared wavelength region, the change of absorption peaks caused by the substitution routinely correspond to 2nd and 3rd overtones and combinations.

In summary, ion (atom) substitution can lead to the variation of absorption peaks compared with corresponding endmembers in the spectral library. The positions of these changed absorption peaks are determined by the type of hosts and guests, and the intensity variation of these peaks are influenced by the amount of substitution [41].

C. Sparsity of spectral variation

In a real geological environment, the number and type of substituted guests vary in different conditions, thus the spectral variation is changeable. It is difficult for traditional methods to address the influence of the spectral variation caused by ion (atom) substitution.

Here, we define redundant spectrum to represent the spectral variation before and after ion (atom) substitution. Since the variation occurs in absorption bands, the redundant spectrum is of sparse property mathematically. For the library-based linear unmixing problem, the spectral signature of each mixed pixel is a linear combination of a handful of pure endmembers in the library. Therefore it can be inferred that the sum of redundant spectra for all endmembers in the mixed pixel remains sparse.

III. SPARSE REDUNDANT UNMIXING MODEL AND ALGORITHM

A. Sparse Redundant Unmixing Model

Suppose $\mathbf{y} \in R^L$ denotes the spectral vector of a mixed pixel, $\mathbf{A} \in R^{L \times m}$ represents the given spectral library, where L is the number of spectral bands and m is the number of pure endmembers in the library. For each pixel,

---

[1]Random motions of any vibrating system are made up from a restricted number of simple motions, which are called the normal vibrations or fundamentals

the sparse redundant unmixing model can be written as

$$\mathbf{y} = \mathbf{A}\mathbf{x} + \mathbf{b} \tag{1}$$

where $\mathbf{x} \in R^m$ is vector of the fractional abundances corresponding to the spectral library, $\mathbf{b} \in R^L$ denotes the mixed redundant spectrum in the pixel.

Due to physical constraints, the model has two constraints (x_i is the ith element of $\mathbf{x}$), i.e.,

$$\mathbf{x} \geq \mathbf{0} \tag{2}$$

$$\sum_{i=1}^{m} x_i = 1 \tag{3}$$

which are also called abundance nonnegativity constraint (ANC) and abundance sum-to-one constraint (ASC), respectively. Since the number of endmembers in one pixel is much smaller than the number of pure endmembers in the ever-growing spectral library, vector $\mathbf{x}$ is supposed to be sparse. Also, the sum of the redundant spectra of endmembers in the pixel, denoted as $\mathbf{b}$, is supposed to be sparse. In real hyperspectral images, due to the strong universal signature variability, the ASC is prone to harsh criticisms in the literature [3, 26]. The ASC should be replaced by a so-called generalized sum-to-one constraint that is automatically imposed because of the nonnegativity of the sources. Therefore, we do not need to add the sum-to-one constraint to the sparse unmixing model.

Here, the model is rewritten as

$$\mathbf{y} = \mathbf{A}\mathbf{x} + \mathbf{b} = \begin{bmatrix} \mathbf{A} & \mathbf{I} \end{bmatrix} \begin{bmatrix} \mathbf{x} \\ \mathbf{b} \end{bmatrix} = \hat{\mathbf{A}}\hat{\mathbf{x}} \tag{4}$$

where

$$\hat{\mathbf{A}} \equiv \begin{bmatrix} \mathbf{A} & \mathbf{I} \end{bmatrix} \tag{5}$$

$$\hat{\mathbf{x}} \equiv \begin{bmatrix} \mathbf{x} \\ \mathbf{b} \end{bmatrix} \tag{6}$$

The optimization problem based on the sparse redundant unmixing model can be expressed as

$$\min_{\hat{\mathbf{x}}} \|\hat{\mathbf{x}}\|_0$$

$$\text{subject to} \quad \|\hat{\mathbf{A}}\hat{\mathbf{x}} - \mathbf{y}\|_2 \leq \delta, \mathbf{x} \geq \mathbf{0} \tag{7}$$

where $\|\hat{\mathbf{x}}\|_0$ denotes the number of nonzero components in $\hat{\mathbf{x}}$, and $\delta \geq 0$ represents the error tolerance. It should be noted that $\mathbf{x}$ is constrained to be positive, while $\mathbf{b}$ (redundant spectrum) can be either positive or negative.

B. Sparse Redundant Unmixing Algorithm

Here, SpaRedU algorithm is introduced to solve optimization problem in (7). Due to the discrete and nonconvex nature of l_0 norm, the problem is NP hard which means that it is combinatorial and too complex to solve. Therefore, it can not be solved in a straightforward way. To get an approximate solution to the problem, several sparse unmixing

algorithms based on greedy method [3, 26, 30], convex relaxation method [25, 28], and sparse Bayesian method [48], have been proposed. One popular strategy is to replace l_0 norm with l_1 norm, since l_1 norm is naturally the best convex approximation of l_0 norm. Therefore the optimization problem in (7) can be converted to

$$\min_{\hat{\mathbf{x}}} \|\hat{\mathbf{x}}\|_1$$
$$\text{subject to} \quad \|\hat{\mathbf{A}}\hat{\mathbf{x}} - \mathbf{y}\|_2 \leq \delta, \mathbf{x} \geq \mathbf{0} \tag{8}$$

With an appropriate Lagrange multiplier, the optimization problem in (8) becomes

$$\min_{\hat{\mathbf{x}}} \frac{1}{2}\|\hat{\mathbf{A}}\hat{\mathbf{x}} - \mathbf{y}\|_2^2 + \lambda\|\hat{\mathbf{x}}\|_1$$
$$\text{subject to} \quad \mathbf{x} \geq \mathbf{0} \tag{9}$$

where λ is regularization parameter.

The optimization problem in (9) is convex and can be solved based on ADMM. An equivalent expression of (9) is

$$\min_{\hat{\mathbf{x}}} \frac{1}{2}\|\hat{\mathbf{A}}\hat{\mathbf{x}} - \mathbf{y}\|_2^2 + \lambda\|\hat{\mathbf{x}}\|_1 + \iota_{\mathbb{R}_+^n}(\mathbf{x}) \tag{10}$$

where $\iota_{\mathbb{R}_+^n}(\mathbf{x})$ is the indicator function, i.e., $\iota_{\mathbb{R}_+^n}(\mathbf{x})$ is zero if $\mathbf{x} \geq \mathbf{0}$ is satisfied and $+\infty$ otherwise.

According to the objective function (10), it can be converted into the equivalent formulation

$$\min_{\hat{\mathbf{x}}, \hat{\mathbf{u}}} \frac{1}{2}\|\hat{\mathbf{A}}\hat{\mathbf{x}} - \mathbf{y}\|_2^2 + \lambda\|\hat{\mathbf{u}}\|_1 + \iota_{\mathbb{R}_+^n}(\mathbf{u})$$
$$\text{subject to} \quad \hat{\mathbf{x}} = \hat{\mathbf{u}} \tag{11}$$

where

$$\hat{\mathbf{u}} \equiv \begin{bmatrix} \mathbf{u} \\ \mathbf{v} \end{bmatrix} \tag{12}$$

$$\mathbf{u} = \mathbf{x} \tag{13}$$

$$\mathbf{v} = \mathbf{b} \tag{14}$$

In the optimization problem (11), $\mathbf{x}$, $\mathbf{b}$ and $\mathbf{u}$, $\mathbf{v}$ are coupled together. The mathematical expression satisfies the ADMM framework and thus can be solved based on ADMM with theoretical convergence.

The augmented Lagrangian for the problem is

$$\mathcal{L}(\hat{\mathbf{x}}, \hat{\mathbf{u}}, \hat{\mathbf{d}}) = \frac{1}{2}\left\|\hat{\mathbf{A}}\hat{\mathbf{x}} - \mathbf{y}\right\|_2^2 + \lambda\|\hat{\mathbf{u}}\|_1 + \iota_{\mathbb{R}_+^n}(\mathbf{u})$$
$$+ \hat{\mathbf{d}}^T(\hat{\mathbf{x}} - \hat{\mathbf{u}}) + \frac{\rho}{2}\|\hat{\mathbf{x}} - \hat{\mathbf{u}}\|_2^2 \tag{15}$$

This equation can be rewritten as

$$\mathcal{L}(\hat{\mathbf{x}}, \hat{\mathbf{u}}, \hat{\mathbf{w}}) = \frac{1}{2}\left\|\hat{\mathbf{A}}\hat{\mathbf{x}} - \mathbf{y}\right\|_2^2 + \lambda\|\hat{\mathbf{u}}\|_1$$
$$+ \iota_{\mathbb{R}_+^n}(\mathbf{u}) + \frac{\rho}{2}\|\hat{\mathbf{x}} - \hat{\mathbf{u}} - \hat{\mathbf{w}}\|_2^2 \tag{16}$$

where

$$\hat{\mathbf{w}} \equiv -\frac{1}{\rho}\hat{\mathbf{d}} \tag{17}$$

Through a careful choice of the new variable, the initial problem is converted into a much simple problem. Given that the optimization is considered over the variable $\hat{\mathbf{x}}$, the optimization function can be reduced to

$$\hat{\mathbf{x}}^{k+1} \leftarrow \arg\min_{\hat{\mathbf{x}}} \frac{1}{2}\left\|\hat{\mathbf{A}}\hat{\mathbf{x}} - \mathbf{y}\right\|_2^2 + \frac{\rho}{2}\left\|\hat{\mathbf{x}} - \hat{\mathbf{u}}^k - \hat{\mathbf{w}}^k\right\|_2^2 \tag{18}$$

The solution of (18) is simply

$$\hat{\mathbf{x}}^{k+1} \leftarrow (\hat{\mathbf{A}}^T\hat{\mathbf{A}} + \rho\mathbf{I})^{-1}\left[\hat{\mathbf{A}}^T\mathbf{y} + \rho(\hat{\mathbf{u}}^k + \hat{\mathbf{w}}^k)\right] \tag{19}$$

where $\mathbf{I}$ is the identity matrix, $\hat{\mathbf{A}}^T$ denotes the transpose of $\hat{\mathbf{A}}$.

In order to calculate $\hat{\mathbf{u}}$, the optimization problem to be solved is

$$\hat{\mathbf{u}}^{k+1} \leftarrow \arg\min_{\hat{\mathbf{u}}} \frac{\lambda}{\rho}\|\hat{\mathbf{u}}\|_1 + \iota_{\mathbb{R}_+^n}(\mathbf{u}) + \frac{1}{2}\left\|\hat{\mathbf{u}} - \hat{\mathbf{z}}^k\right\|_2^2 \tag{20}$$

where

$$\hat{\mathbf{z}}^k \equiv \hat{\mathbf{x}}^{k+1} - \hat{\mathbf{w}}^k \tag{21}$$

Here, we define

$$\hat{\mathbf{z}}^k \equiv \begin{bmatrix} \mathbf{z}_1^k \\ \mathbf{z}_2^k \end{bmatrix} \tag{22}$$

$$\hat{\mathbf{w}}^k \equiv \begin{bmatrix} \mathbf{w}_1^k \\ \mathbf{w}_2^k \end{bmatrix} \tag{23}$$

$$\mathbf{z}_1^k \equiv \mathbf{x}^{k+1} - \mathbf{w}_1^k \tag{24}$$

$$\mathbf{z}_2^k \equiv \mathbf{b}^{k+1} - \mathbf{w}_2^k \tag{25}$$

Without considering the term $\iota_{\mathbb{R}_+^n}(\mathbf{u})$, the solution of optimization problem in (20) is the well-known soft threshold.

$$\hat{\mathbf{u}}^{k+1} \leftarrow soft(\hat{\mathbf{z}}^k, \frac{\lambda}{\rho}) \tag{26}$$

The above solution of optimization problem can also be written as

$$\begin{bmatrix} \mathbf{u}^{k+1} \\ \mathbf{v}^{k+1} \end{bmatrix} \leftarrow soft(\begin{bmatrix} \mathbf{z}_1^k \\ \mathbf{z}_2^k \end{bmatrix}, \frac{\lambda}{\rho}) \tag{27}$$

$$\mathbf{u}^{k+1} \leftarrow soft(\mathbf{z}_1^k, \frac{\lambda}{\rho}) \tag{28}$$

$$\mathbf{v}^{k+1} \leftarrow soft(\mathbf{z}_2^k, \frac{\lambda}{\rho}) \tag{29}$$

The solution is projected onto the first orthant because of the effect of the abundance nonnegativity constraint (ANC) term $\iota_{\mathbb{R}_+^n}(\mathbf{u})$

Algorithm 1 Pseudocode of the SpaRedU algorithm

1: **Initialization:**

2:     set $k = 0$, $\rho \geq 0$, $\hat{\mathbf{x}}^0$, $\hat{\mathbf{u}}^0$, $\hat{\mathbf{w}}^0$

3: **Repeat:**

4:     $\hat{\mathbf{x}}^{k+1} \leftarrow \arg\min_{\hat{\mathbf{x}}} \frac{1}{2} \left\| \hat{\mathbf{A}}\hat{\mathbf{x}} - \mathbf{y} \right\|_2^2 + \frac{\rho}{2} \left\| \hat{\mathbf{x}} - \hat{\mathbf{u}}^k - \hat{\mathbf{w}}^k \right\|_2^2$

      $\hat{\mathbf{x}}_{k+1} \leftarrow (\hat{\mathbf{A}}^T\hat{\mathbf{A}} + \rho\mathbf{I})^{-1} \left[\hat{\mathbf{A}}^T\mathbf{y} + \rho(\hat{\mathbf{u}}^k - \hat{\mathbf{w}}^k) \right]$

5:     $\hat{\mathbf{z}}^k \equiv \hat{\mathbf{x}}_{k+1} - \hat{\mathbf{w}}^k$

6:     $\hat{\mathbf{u}}^{k+1} \leftarrow \arg\min_{\hat{\mathbf{u}}} \frac{\lambda}{\rho} \|\hat{\mathbf{u}}\|_1 + \iota_{\mathbb{R}_+^n}(\mathbf{u}) + \frac{1}{2} \left\| \hat{\mathbf{u}} - \hat{\mathbf{z}}^k \right\|_2^2$

      $\hat{\mathbf{u}}^{k+1} \leftarrow \begin{bmatrix} \left\{ \mathbf{0}, soft(\mathbf{z}_1^k, \frac{\lambda}{\rho}) \right\} \\ soft(\mathbf{z}_2^k, \frac{\lambda}{\rho}) \end{bmatrix}$

7: **Update Lagrange multipliers:**

      $\hat{\mathbf{w}}^{k+1} \leftarrow \hat{\mathbf{w}}^k - (\hat{\mathbf{x}}^{k+1} - \hat{\mathbf{u}}^{k+1})$

8: **Update iteration:** $k \leftarrow k + 1$

9: **Until** some stopping criterion is satisfied

$$\mathbf{u}_{k+1} \leftarrow \max \left\{ \mathbf{0}, soft(\mathbf{z}_1^k, \frac{\lambda}{\rho}) \right\} \tag{30}$$

$$\mathbf{v}^{k+1} \leftarrow soft(\mathbf{z}_2^k, \frac{\lambda}{\rho}) \tag{31}$$

Lagrange multipliers update to

$$\hat{\mathbf{w}}^{k+1} \leftarrow \hat{\mathbf{w}}^k - (\hat{\mathbf{x}}^{k+1} - \hat{\mathbf{u}}^{k+1}) \tag{32}$$

The detailed process for SpaRedU is shown in Algorithm 1.

Concerning the computational complexity of SpaRedU, the most costly expensive steps are the calculus of $\mathbf{x}$. Since the rank of matrix $(\mathbf{A}^T\mathbf{A} + \rho_1\mathbf{I})$ is no larger than the number of bands, $(\mathbf{A}^T\mathbf{A} + \rho_1\mathbf{I})^{-1}$ can be easily precomputed. The calculus of $\mathbf{x}$ has the order of complexity $\mathcal{O}(m^2)$, while other computation has smaller computational complexity. The complexity of the algorithm per iteration is thus $\mathcal{O}(m^2)$, which corresponds to the matrix-vector products and has the same theoretical complexity as SUnSAL [28].

IV. SIMULATION EXPERIMENT

Ion (atom) substitution in the geological process is prevalent in practice. Therefore, in this section, spectral data containing redundant information are designed to approximate spectra in the real environment. The experiment is then conducted on simulated data to analyze the influence of the redundant spectrum on the unmixing results. Here, the performance of SpaRedU is compared with that of SMP, SUnSAL, SUnSAL-TV, and DANSER.

This section is organized as follows: Section IV-A describes the performance discriminator. Section IV-B presents the spectral library used in simulated data. Section IV-C shows how the simulated data set is generated. Section IV-D presents the results and discussion in the simulation experiment.

A. Performance Discriminators

The root mean square error (RMSE) is used to measure the reconstruction quality of spectral signature. For the i-th endmember, RMSE is defined as

$$\text{RMSE}_i \equiv \sqrt{\frac{1}{K} \sum_{j=1}^{K} (\mathbf{x}_i^j - \tilde{\mathbf{x}}_i^j)^2}. \tag{33}$$

where $\mathbf{x}_i^j$ represents the true fractional abundance of the i-th endmember in the j-th pixel and $\tilde{\mathbf{x}}_i^j$ denotes the estimated one, K represents the number of pixels in the hyperspectral data.

The performance discriminator RMSE_i measures the reconstruction quality of the fractional abundances of the i-th endmember in all pixels. The mean value of RMSE for all the endmembers will be calculated. Generally, smaller RMSE means more accurate estimation.

B. Spectral Library

The spectral library $\mathbf{A} \in R^{224 \times 498}$ used in the simulation experiment contains 498 spectral signatures from the United States Geological Survey (USGS)[2] released in September 2007 [39]. The reflectance values of the spectral library $\mathbf{A}$ are measured in 224 spectral bands distributed uniformly in the range of $0.4 - 2.5\mu m$.

C. Simulated Data Set

Here, four spectral signatures are selected from spectral library $\mathbf{A}$ to generate the simulated hyperspectral images: Jarosite JR2501 K, Clinochlore GDS159, Analcime GDS1 and Chrysocolla HS297.3B. In the real environment, due to the physical and chemical variation, the first two materials usually occur ion (atom) substitution. Specifically, for Jarosite JR2501 K, Na^+ can substitute for K^+, while Fe^{2+} can replace Mg^{2+} in Clinochlore GDS159 under appropriate condition. Based on the analysis of spectral variation, the redundant spectrum is sparse and related to the type and amount of host and guest ions (atoms). In general, the variation of spectra after the substitution usually occurs at the bands of absorption peaks of host and guest ions (atoms) and the varied intensity of absorption peaks is determined by the substitution amount.

To testify the validity of the SpaRedU algorithm, the spectra after substitution should be simulated based on the above description. As for Jarosite, when the amount of substitutional Na is higher than that of residual K, it would convert to Natrojarosite. The spectra of these two materials are included in spectral library $\mathbf{A}$. Compared with these two spectra, one can roughly estimate the bands of varied absorption peaks and obtain the tendency of varied intensity (as shown in Fig. 2 (a)). As shown in Fig. 2 (a), during the ion (atom) substitution, the spectrum of Jarosite changes in different absorption bands. Specifically, the reflectance value decreases significantly around wavelength of 1.0, 1.52, 1.6, 1.89 and 2.28 μm. Thus, we regard these wavelength locations as the varied absorption bands. After identifying the location of varied absorption bands, we can roughly get the reflectance difference of the two spectra. The measurement of the exact reflectance difference in hyperspectral scene is very difficult. Since

---

[2]Available online: http://speclab.cr.usgs.gov/spectral-lib.html

the reflectance variation of absorption band changes linearly with the amount of ion substitution, here we manually set the varied intensity as 30 percent of the total corresponding difference values of the two spectral signatures to generate the spectrum of the changed Jarosite (shown in Fig. 2 (b)).

To simulate the spectra of materials after substitution, proper Gaussian distribution functions are used to approximate the reflectance difference of absorption peaks. The reason of using Gaussian distribution function is that Gaussian curve is very similar to the spectral variation. Besides, Gaussian distribution function can be tuned easily. Specifically, Gaussian distribution function is shown as follows

$$f(x|\mu,\sigma^2) = \frac{1}{\sqrt{2\sigma^2\pi}}e^{-\frac{(x-\mu)^2}{2\sigma^2}} \tag{34}$$

where μ is the mean of the distribution, σ is the standard deviation and σ^2 is the variance. By adjusting μ, we can change the locations of peaks, making them in accordance with the varied absorption peaks of spectra. Then, we can adjust σ to make the shape of Gaussian curve similar to the curve near the absorption band.

In the simulation experiment, five Gaussian distribution functions are used to simulate the spectral variation caused by ion (atom) substitution (shown in Fig. 2 (b)).

$$F(x) = \sum_{i=1}^{5} \lambda_i f(x|\mu_i,\sigma_i^2) \tag{35}$$

where μ_i is the mean of the distribution, σ_i is the standard deviation, σ_i^2 is the variance and λ_i is the weight of each Gaussian distribution function.

Here, the parameters of each Gaussian distribution function are tuned mannually. By adjusting the parameters (μ_i, σ_i and λ_i) of each Gaussian distribution function, we can obtain the approximate spectral variation caused by ion (atom) substitution successfully (shown in Fig. 2 (b)).

Likewise, the spectra of Clinochlore after substitution can be obtained using similar strategy. For Analcime and Chrysocolla, their pure spectra in the library are directly used in the simulation experiment. Next, the above four spectral signatures are used to generate a simulated hyperspectral imagery with 64×64 pixels (224 bands per pixel).

The simulated data is generated by mixing linearly the above four pure endmembers. The generation procedure of the simulated data is as follows [30].

1) Divide the scene from its original size ($t^2 \times t^2 (t = 8)$) into several $t \times t$ regions. Then initialize each region with the same type of ground cover randomly selected from the above four endmembers. The size of spectral signature matrix W is $L \times P(L = 224)$, where P is the endmember number.

2) Create mixed pixels using a $(t+1) \times (t+1)$ spatial low-pass filter.

3) To further remove pure pixels and represent the sparseness of abundances, all the pixels where the abundance of a single endmember is larger than 80% are substituted by a mixture which consists of only two endmembers (the abundances of the two endmembers both equal to 50%). After the three steps, we obtain the distribution of P endmembers in the scene, and specific values are stored in H with a size of $P \times K(K = t^2 \times t^2)$.

4) Use linear mixing model $Y = W \times H$ to generate hyperspectral data, and add Gaussian white noise[3] with

[3]The Gaussian white noise is generated using the *awgn* function in MATLAB.
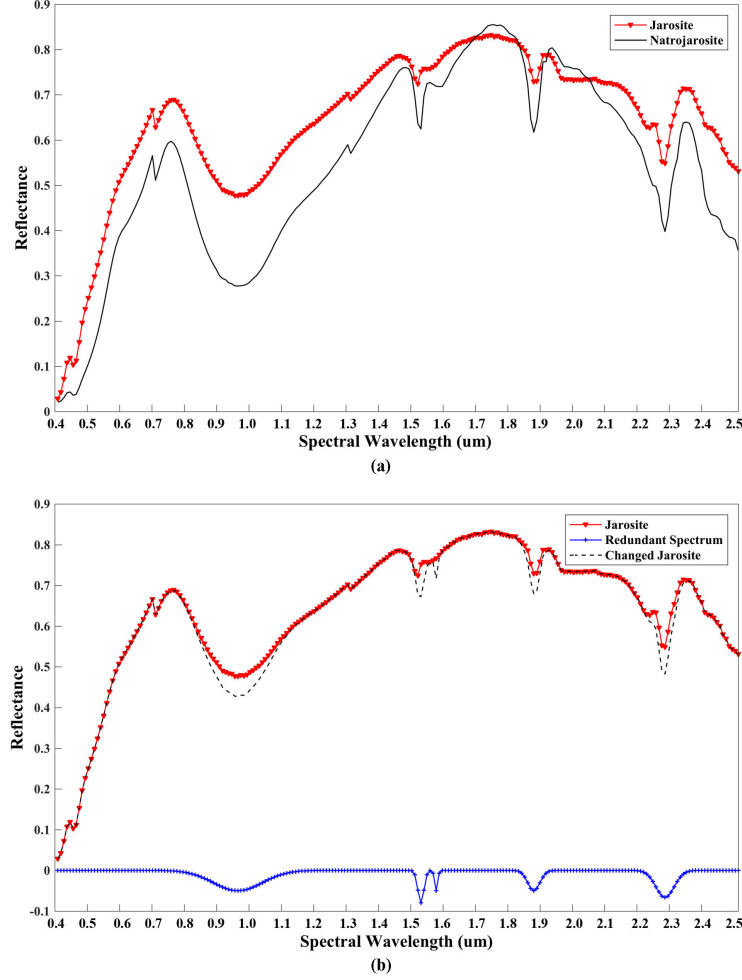
Fig. 2. (a) Comparison of spectral signatures of Jarosite and Natrojarosite. (b) Spectral signatures of Jarosite after considering redundant spectrum.

specific signal-to-noise ratio (SNR $\equiv 10 \log_{10}(\frac{\mathbb{E}[\|\mathbf{Ax}\|_2^2]}{\mathbb{E}[\|\mathbf{n}\|_2^2]})$) at the same time.

D. Results and Discussion

This part shows the unmixing performance of SpaRedU on the simulated data compared with SMP, SUnSAL, SUnSAL-TV and DANSER.

Fig. 3 shows the abundance maps of all four selected endmembers obtained by the considered methods. Since the results under different noise levels exhibit similar conclusion, only the near-optimal results observed under SNR = 40 dB are presented. Compared with the true abundance maps, it can be seen in Fig. 3 that SpaRedU is able to recover the fractional abundances of all the four endmembers with more accurate results. In contrast, other algorithms cannot achieve comparable abundance estimation especially on the two left endmembers whose spectral signatures are influenced by the ion (atom) substitution.
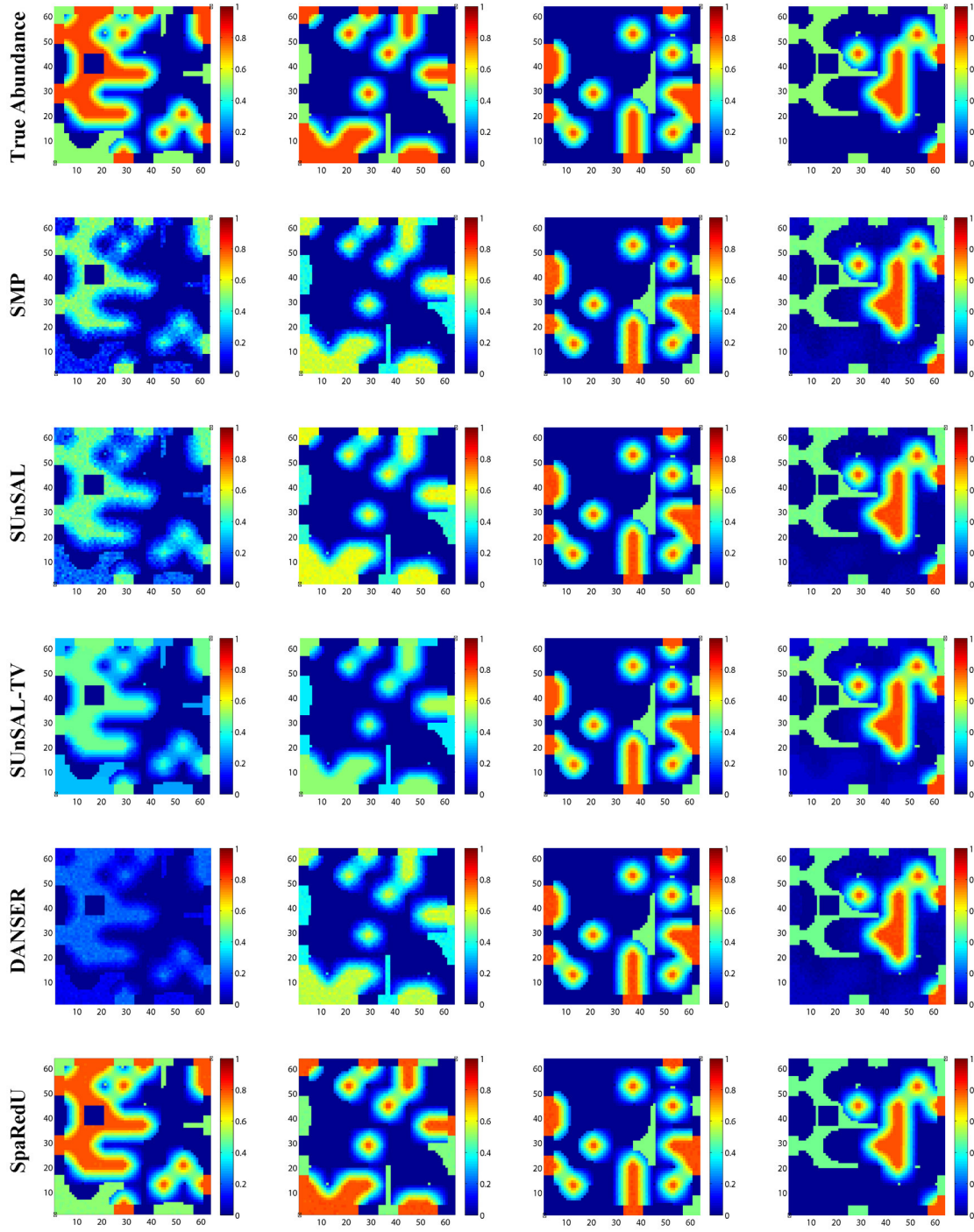
Fig. 3. Comparison of abundance maps on simulated data with 40 dB white noise. From top to bottom row are true abundance maps, abundance maps obtained by SMP, abundance maps obtained by SUnSAL, abundance maps obtained by SUnSAL-TV, abundance maps obtained by DANSER, and abundance maps obtained by SpaRedU, respectively. Columns from left to right are the abundance maps for four endmembers, respectively.

TABLE I

RMSEs OBTAINED BY CONSIDERED ALGORITHMS ON THE SIMULATED DATA (THE VALUES OF OPTIMAL PARAMETERS FOR CONSIDERED ALGORITHMS ARE INDICATED IN THE PARENTHESES)

SNR (dB)	SMP	SUnSAL	SUnSAL-TV	DANSER	SpaRedU
20	0.2394	0.2564	0.2445	0.2430	**0.1358**
		$(\lambda = 0.2)$	$(\lambda = 0.010, \lambda_{TV} = 0.020)$		$(\lambda = 0.200)$
30	0.1172	0.1789	0.1273	0.1255	**0.0742**
		$(\lambda = 0.03)$	$(\lambda = 0.005, \lambda_{TV} = 0.006)$		$(\lambda = 0.060)$
40	0.1095	0.1296	0.1010	0.1290	**0.0290**
		$(\lambda = 0.007)$	$(\lambda = 0.002, \lambda_{TV} = 0.002)$		$(\lambda = 0.040)$
50	0.0992	0.1181	0.0998	0.1284	**0.0203**
		$(\lambda = 0.003)$	$(\lambda = 0.002, \lambda_{TV} = 0.001)$		$(\lambda = 0.030)$

Table I shows the RMSE values achieved by the considered methods under all considered SNR levels (20, 30, 40 and 50 dB). The Table only shows the near-optimal results by using optimal parameters. In order to find the near-optimal parameters for each considered method, a large range of possible discrete values of parameters are considered. It can be seen that the performances of all the methods upgrade as the noise gets weaker. From Table I, it can be observed that, SpaRedU generally obtains smaller RMSE values compared with other algorithms. The result confirms that imposing the sparse redundant regularizer can lead to the improved performance in hyperspectral unmixing.

Table II shows the RMSE values achieved by the considered methods for each endmember. The RMSE values shown in the Table are achieved by using optimal parameters for the simulated data (SNR = 40dB). It can be observed that the RMSE values obtained by SpaRedU are much lower than the values in other algorithms, especially for Jarosite and Clinochlore. Therefore, the performance of SpaRedU is much better than other algorithms, which are also in line with the results displayed in Fig. 3.

Fig. 4 indicates true and the estimated redundant spectra of all pixels in the simulated scene (SNR = 40dB). It can be seen that the estimated redundant spectra obtained by SpaRedU are consistent with the true redundant spectra in simulated data. Therefore, SpaRedU can effectively estimate the redundant spectra caused by ion (atom) substitution.

In simulation experiment, it can be concluded that SpaRedU can effectively solve the spectral variation problem caused by the substitution. Compared with other algorithms, SpaRedU can significantly improve unmixing results. Due to the complexity of real hyperspectral imagery, it is necessary to further conduct experiment with real hyperspectral data to testify our conclusion.

TABLE II

RMSEs OBTAINED BY DIFFERENT ALGORITHMS FOR EACH ENDMEMBER ON THE SIMULATED DATA

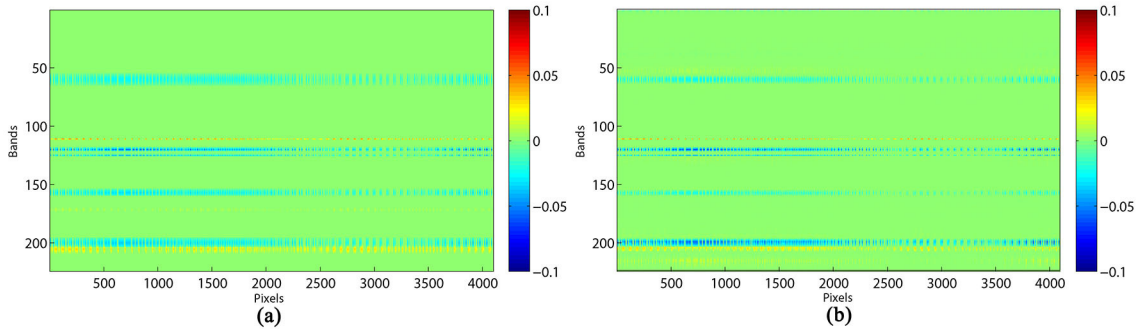|	SMP	SUnSAL ($\lambda = 0.007$)	SUnSAL-TV ($\lambda = 0.002, \lambda_{TV} = 0.002$)	DANSER	SpaRedU ($\lambda = 0.040$)
Jarosite	0.2488	0.2861	0.2026	0.3556	**0.0479**
Clinochlore	0.1397	0.1730	0.1505	0.1202	**0.0465**
Analcime	0.0180	0.0207	0.0147	0.0127	**0.0113**
Chrysocolla	0.0314	0.0387	0.0363	0.0274	**0.0104**

Fig. 4. True (a) and the estimated (b) redundant spectra of the simulated scene (SNR = 40dB).

V. REAL DATA EXPERIMENT

In this section, real data experiment is conducted on the well-known AVIRIS Cuprite data set[4] to test the efficacy of sparse unmixing algorithms. In the AVIRIS Cuprite data set, many minerals, such as Alunite, Jarosite, Calcite, and Montmorillonite, have the ion (atom) substitution phenomenon. Therefore, it should be verified that the redundant spectra obtained by SpaRedU is consistent with the theoretical analysis in section II-A. Meanwhile, it is also necessary to compare the estimated fractional abundances obtained by different sparse unmixing algorithms. As the true abundance maps do not exist, we resort to the classification maps of the real hyperspectral image to make a qualitative analysis. For visual comparison, we display the abundance maps estimated by the SMP, SUnSAL, SUnSAL-TV, DANSER and SpaRedU. The parameter in SUnSAL is set to $\lambda = 0.001$, the parameters in SUnSAL-TV are set to $\lambda = 0.01$, $\lambda_{TV} = 0.003$ and the parameters in SpaRedU are set to $\lambda = 0.01$ (after empirical optimization).

Here, a 204×151 pixels subset of the AVIRIS Cuprite data set is used to test the performance of SMP, SUnSAL, SUnSAL-TV, DANSER and SpaRedU. The scene comprises 224 spectral bands between 0.4 and $2.5 \mu m$, with

---

[4]http://aviris.jpl.nasa.gov/html/aviris.freedata.html

nominal spectral resolution of $10nm$. Absorption bands at spectral wavelength of $0.4 - 0.42\mu m$, $1.38 - 1.47\mu m$, $1.8 - 1.99\mu m$, and $2.48 - 2.5\mu m$ were removed due to water absorption and low SNR, leaving a total of 188 spectral bands. The library $\mathbf{A}_1 \in R^{188 \times 498}$ considered in this section contains 498 materials (different mineral types) from the USGS [39] library denoted splib06[5].

For the absorption bands that are near the discontinuous points, their SNR are usually lower (larger noise) than other absorption bands. Since the number of these low-SNR bands is less than the whole spectral bands, such large noises at these low-SNR bands are sparsely distributed. In this situation, these noises also satisfy the sparse property of the redundant spectra. Thus, our model may also learn these noises at low-SNR bands as a part of redundant spectra, which is a limitation of our model.

For illustrative purpose, Fig. 5 shows a mineral map produced by USGS in 1995, in which the Tricorder 3.3 software was used to map different minerals. Tricorder maps[6] are classification maps, which are different from the estimated abundance maps denoting the proportion of each mineral in mixed pixels. It is noteworthy that the Tricorder map was collected in 1995, while the publicly available AVIRIS Cuprite data was collected in 1997. Therefore, a direct comparison between the 1995 USGS map and the 1997 AVIRIS data is not possible. However, since the true abundance maps do not exist, it is reasonable to make a qualitative assessment of the results obtained by the considered methods through the comparison with the USGS classification map.

To verify the property of the redundant spectra in real hyperspectral data, we select minerals with high abundance, such as Alunite, Calcite, and Muscovite, from AVIRIS Cuprite data to discuss where the spectral variation occurs. In Alunite, K^+ can be substituted by Na^+. For Calcite, Ca^{2+} can be substituted by Ba^{2+}, Mg^{2+}, Fe^{2+}, Mn^{2+} under appropriate conditions. In Muscovite, Al^{3+} can be substituted by other ions like Fe^{3+}, Mg^{2+}, Fe^{2+}, and so on. Physically, such ion (atom) substitution results in the spectral variation of specific absorption peaks. Therefore, they are eligible to be served as a justification of redundant spectrum.

Theoretically, non-zero band in redundant spectra does not exist in all pixels of the hyperspectral scene. For the whole scene, it exists in those pixels which contain minerals that have ion (atom) substitution. Here, we exclusively analyze the redundant spectra of pixels where such minerals are involved. The widely-distributed Alunite is used as an example to discuss the spectral variation and redundant spectrum.

Firstly, the spectral variation of Alunite is analyzed. In Alunite, K^+ can be substituted by Na^+. Fig. 6 shows the spectra of Alunite GDS84 Na03, and Alunite GDS82 Na82. The former scarcely has Na^+, while the latter has much more Na^+ because of $K^+ - Na^+$ substitution in Alunite. In Fig. 6, absorption bands at spectral wavelength of $0.4 - 0.42\mu m$, $1.38 - 1.47\mu m$, $1.8 - 1.99\mu m$, and $2.48 - 2.5\mu m$ were removed due to water absorption and low SNR.

As shown in Fig. 6, through ion (atom) substitution, the spectrum of Alunite changes in different absorption bands. Specifically, as the amount of substituted Na^+ increases, the reflectance value decreases significantly around

[5]http://speclab.cr.usgs.gov/spectral.lib06

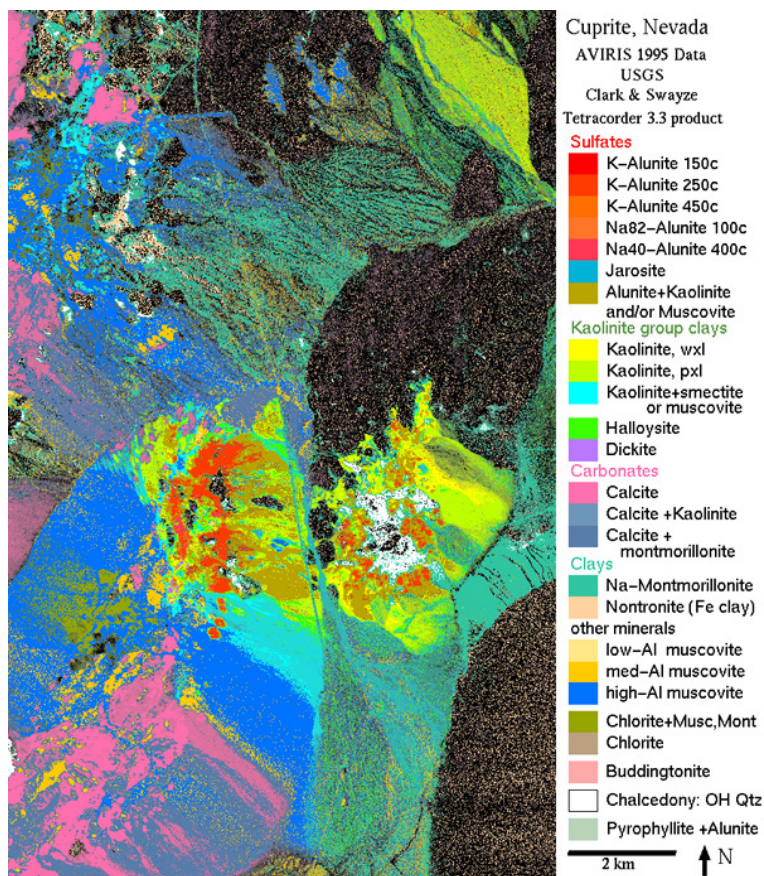[6]http://speclab.cr.usgs.gov/PAPER/tetracorder

Fig. 5. USGS map showing the distribution of different minerals in the Cuprite mining district in Nevada.
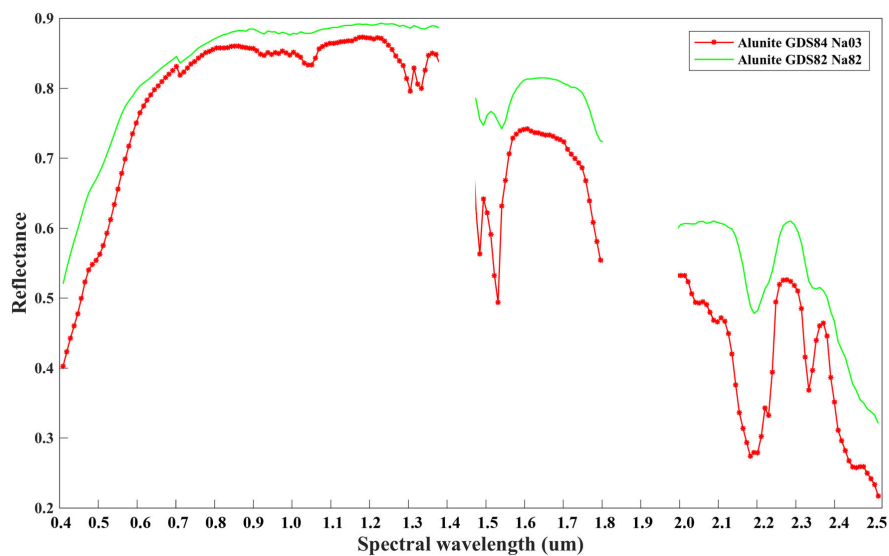

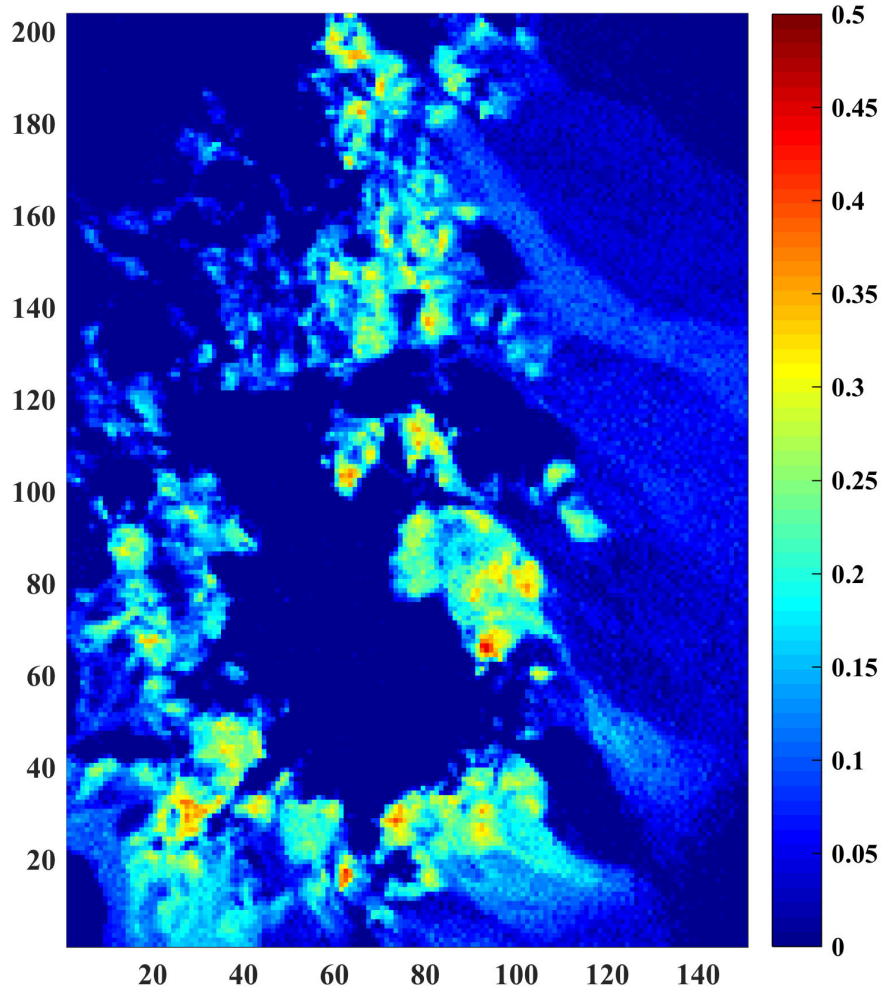Fig. 6. The spectra of Alunite GDS84 Na03, and Alunite GDS82 Na82.

Fig. 7. The abundance map of Alunite in our proposed method.

wavelengths of 1.03, 1.3, 1.32, 1.52, 2.18, and 2.32 μm. Thus, we regard these wavelength locations as the varied absorption bands caused by ion (atom) substitution.

Secondly, the redundant spectra of pixels that contain Alunite in the scene is discussed. Fig. 7 shows the abundance map of the Alunite obtaned by SpaRedU. From Fig. 7, we can easily identify the coordinates of pixels that contain Alunite. Here, we extract the coordinates of pixels whose abundance of Alunite are at top 1% (300 pixels) in the scene. The redundant spectra of these extracted pixels are shown in Fig. 8. It can be observed that the location of varied absorption peaks shown in Fig. 6 are in accordance with the non-zero bands of redundant spectra shown in Fig. 8.

Therefore, it can be observed that the varied absorption peaks of minerals that have ion (atom) substitution are nearly the same with the nonzero bands in the redundant spectra, which is consistent with the theoretical analysis
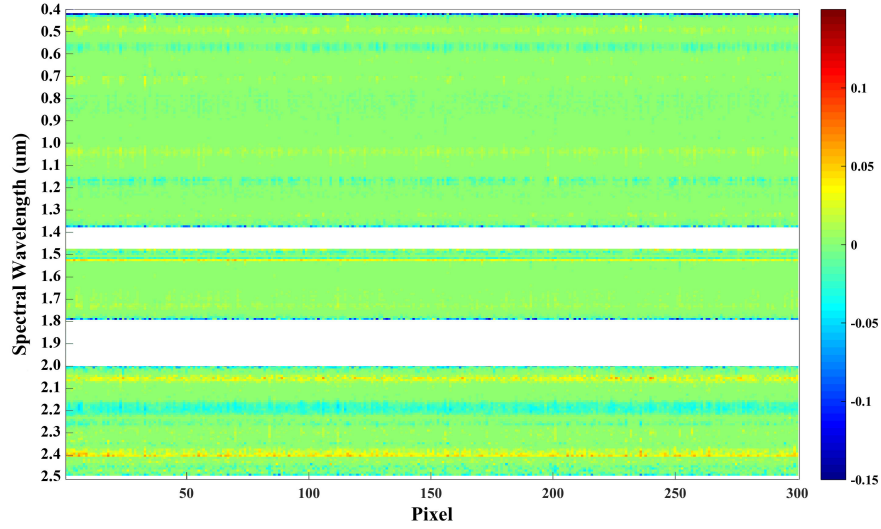
Fig. 8. The redundant spectra of the 300 pixels whose abundance of Alunite are about top 1% of all pixels in the scene.

in previous section.

Fig. 9 shows the distribution maps produced by Tricorder software and the abundance maps obtained by SMP, SUnSAL, SUnSAL-TV, SANSER and SpaRedU for four endmembers (i.e. Alunite, Buddingtonite, Chalcedony and Montmorillonite) in the AVIRIS Cuprite scene. Regardless of the difference between the Tricorder maps and the abundance maps estimated by the considered algorithms, it can be observed that the relatively high abundances of the four minerals in each algorithm are generally in accordance with corresponding minerals in the Tricorder maps. Therefore, SpaRedU is an effective algorithm for sparse unmixing in the real hyperspectral scene. Besides, the abundances estimated by SpaRedU are comparable or higher than the corresponding ones obtained by other algorithms.

In summary, this section demonstrates that SpaRedU algorithm can effectively solve the spectral variation problem caused by ion (atom) substitution in real hyperspectral imagery. The property of redundant spectra obtained by SpaRedU is consistent with the theoretical analysis of spectral variation. Besides, the abundance result in real experiment is in line with those of the simulation experiment, which indicates that the inclusion of the redundant information in sparse unmixing can help improve the abundance estimation.

VI. Conclusion

In this paper, we study the influence of spectral variation caused by ion (atom) substitution on the hyperspectral unmixing. We propose a sparse unmixing model including redundant information, and develop SpaRedU algorithm to solve the new model. Simulation experiment demonstrates that SpaRedU algorithm, which exploits the spectral redundant information, can effectively solve the spectral variation problem caused by the substitution. Specifically, the estimated redundant spectra by SpaRedU are consistent with the designed one in the simulation experiment.
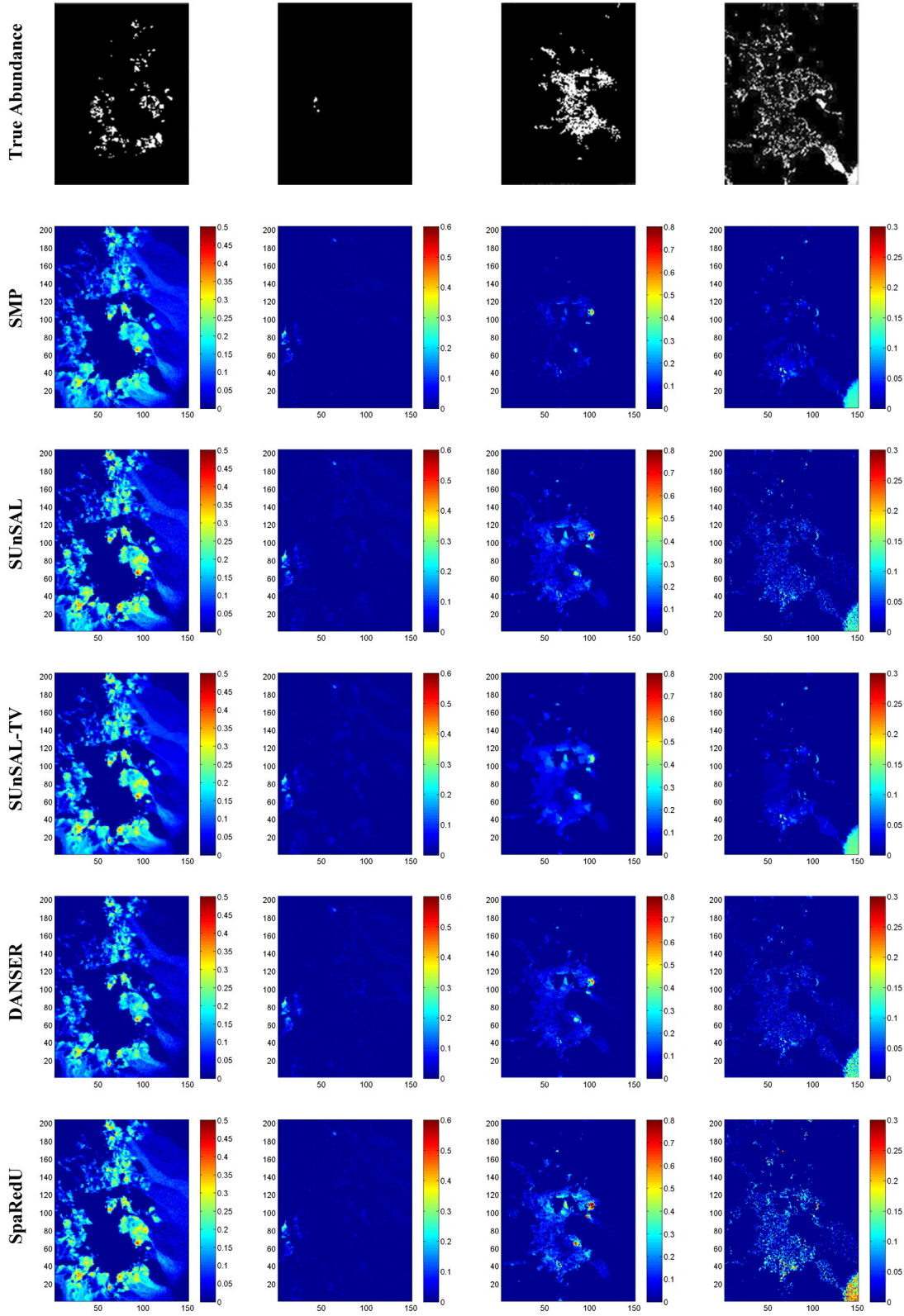
Fig. 9. The distribution maps produced by Tricorder software and the abundance maps estimated by SMP, SUnSAL, SUnSAL-TV, DANSER and SpaRedU. From left to right column are the maps corresponding to Alunite, Buddingtonite, Chalcedony and Montmorillonite, respectively.

Besides, the abundance estimation of endmembers can be improved by using SpaRedU compared with other algorithms. Real data experiment demonstrates that the redundant spectra obtained by SpaRedU is consistent with the theoretical analysis of spectral variation. The performance of SpaRedU in real data experiment also verifies that it can effectively obtain the abundance estimation.

In the future work, to further improve the proposed SpaRedU, the spatial-contextual information of redundant spectra can be explored by adding the total variation (TV) regularization of redundant spectra to our model.

REFERENCES

[1] A. Plaza, J. Benediktsson, J. Boardman, J. Brazile, L. Bruzzone, G. Camps-Valls, J. Chanussot, M. Fauvel, P. Gamba, A. Gualtieri, M. Marconcini, J. Tilton, and G. Trianni. "Recent advances in techniques for hyperspectral image processing," *Remote Sens. Environ.*, vol. 113, pp. 110–122, Sept. 2009.

[2] R. Green, M. Eastwood, C. Sarture, T. Chrien, M. Aronsson, B. Chippendale, J. Faust, B. Pavri, C. Chovit, M. Solis, et al. "Imaging spectroscopy and the airborne visible/infrared imaging spectrometer (AVIRIS)". *Remote Sens. Environ.*, vol. 65, no. 3, pp. 227–248, Sept. 1998.

[3] M. D. Iordache, J. M. Bioucas-Dias, and A. Plaza, "Sparse unmixing of hyperspectral data," *IEEE Trans. Geosci. Remote Sens.*, vol. 49, no. 6, pp. 2014–2039, Jun. 2011.

[4] B. Pan, Z. Shi, Z. An, Z. Jiang, and Y. Ma, "A Novel Spectral-Unmixing-Based Green Algae Area Estimation Method for GOCI Data," *IEEE J. Sel. Top. Appl. Earth Obs. Remote Sens.*, vol. 10, no. 2, pp. 437–449, Feb. 2017.

[5] R. Heylen, M. Parente, and P. Gader, "A Review of Nonlinear Hyperspectral Unmixing Methods," *IEEE J. Sel. Top. Appl. Earth Obs. Remote Sens.*, vol. 7, no. 6, pp. 1844–1868, Jun. 2014.

[6] A. Plaza, P. Martinez, R. Perez, and J. Plaza, "A quantitative and comparative analysis of endmember extraction algorithms from hyperspectral data," *IEEE Trans. Geosci. Remote Sens.*, vol. 42, no. 3, pp. 650–663, Mar. 2004.

[7] Q. Du, N. Raksuntorn, N. Younan, and R. King, "End-member extraction for hyperspectral image analysis," *Appl. Opt.*, vol. 47, no. 28, pp. 77–84, Jul. 2008.

[8] D. Heinz and C.-I. Chang, "Fully constrained least squares linear mixture analysis for material quantification in hyperspectral imagery," *IEEE Trans. Geosci. Remote Sens.*, vol. 39, no. 3, pp. 529–545, Mar. 2001.

[9] Y. Altmann, S. McLaughlin, and A. Hero, "Robust Linear Spectral Unmixing Using Anomaly Detection," *IEEE Trans. Comput. Imaging*, vol. 1, no. 2, pp. 74–85, Jun. 2015.

[10] Y. Altmann, N. Dobigeon, S. McLaughlin, and J.-Y. Tourneret, "Residual component analysis of hyperspectral images–application to joint nonlinear unmixing and nonlinearity detection," *IEEE Trans. Image Process.*, vol. 23, no. 5, pp. 2148–2158, May 2014.

[11] Y. Altmann, M. Pereyra, and S. McLaughlin, "Bayesian Nonlinear Hyperspectral Unmixing With Spatial Residual Component Analysis," *IEEE Trans. Comput. Imaging*, vol. 1, no. 3, pp. 174–185, Sep. 2015.

[12] N. Yokoya, J. Chanussot, A. Lwasaki, "Nonlinear unmixing of hyperspectral data using semi-nonnegative matrix factorization," *IEEE Trans. Geosci. Remote Sens.*, vol. 52, no. 2, pp. 1430–1437, Feb. 2014.

[13] Y. Hu, H. Lee, and F. Scarpace, "Optimal linear spectral unmixing," *IEEE Trans. Geosci. Remote Sens.*, vol. 37, no. 1, pp. 639–644, 1999.

[14] M. Berman, H. Kiiveri, R. Lagerstrom, A. Ernst, R. Dunne, and J. Huntington, "ICE: A statistical approach to identifying endmembers in hyperspectral images," *IEEE Trans. Geosci. Remote Sens.*, vol. 42, no. 10, pp. 2085–2095, Oct. 2004.

[15] F. Schmidt, A. Schmidt, E. Treandguier, M. Guiheneuf, S. Moussaoui, and N. Dobigeon, "Implementation strategies for hyperspectral unmixing using Bayesian source separation," *IEEE Trans. Geosci. Remote Sens.*, vol. 48, no. 11, pp. 4003–4013, Nov. 2010.

[16] Y. Qian, S. Jia, J. Zhou, and A. Robles-Kelly, "Hyperspectral unmixing via $l_{1/2}$ sparsity-constrained nonnegative matrix factorization," *IEEE Trans. Geosci. Remote Sens.*, vol. 49, no. 11, pp. 4282–4297, Nov. 2011.

[17] Z. Zhang, Z. Shi, W. Tang and L. Liu. "Hyperspectral unmixing using nonnegative matrix factorization with an approximate L_0 sparsity constraint." *Inter. 5rd CISP*, pp. 1214–1218, Chongqing, China, Oct. 16-18, 2012.

[18] M. Zortea and A. Plaza, "A quantitative and comparative analysis of different implementations of N-FINDR: A fast endmember extraction algorithm," *IEEE Geosci. Remote Sens. Lett.*, vol. 6, no. 4, pp. 787–791, Oct. 2009.

[19] X. Chen, J. Chen, X. Jia, B. Somers, J. Wu, and P. Coppin, "A quantitative analysis of virtual endmembers' increased impact on the collinearity effect in spectral unmixing." *IEEE Trans. Geosci. Remote Sens.*, vol. 49, no. 8, pp. 2945–2956, Aug. 2011.

[20] J. M. Bioucas-Dias, A. Plaza, N. Dobigeon, M. Parente, Q. Du, P. Gader, and J. Chanussot, "Hyperspectral unmixing overview: Geometrical, statistical, and sparse regression-based approaches," *IEEE J. Sel. Topics Appl. Earth Observ. Remote Sens.*, vol. 5, no. 2, pp. 354–379, Apr. 2012.

[21] J. B. Greer, "Sparse demixing of hyperspectral images," *IEEE Trans. Image Process.*, vol. 21, no. 1, pp. 219–228, Jan. 2012.

[22] M. Iordache, "A sparse regression approach to hyperspectral unmixing," *Universidade Técnica de Lisboa, PhD thesis*, 2011.

[23] J. Bieniarz, E. Aguilera, X. X. Zhu, R. Muller, P. Reinartz, "Joint Sparsity Model for Multilook Hyperspectral Image Unmixing", *IEEE Geosci. Remote Sens. Lett.*, vol. 12, no. 4, pp. 696–700, Apr. 2015.

[24] M. Elad, *Sparse and redundant representations. Springer*, 2010.

[25] W. Tang, Z. Shi, Y. Wu, and C. Zhang, "Sparse unmixing of hyperspectral data using spectral a priori information," *IEEE Trans. Geosci. Remote Sens.*, vol. 53, no. 2, pp. 770–783, Feb. 2015

[26] W. Tang, Z. Shi, and Y. Wu, "Regularized simultaneous forward-backward greedy algorithm for sparse

unmixing of hyperspectral data," *IEEE Trans. Geosci. Remote Sens.*, vol. 52, no. 9, pp. 5271–5288, Sep. 2014.

[27] X. Xu, Z. Shi, "Xia Xu, Zhenwei Shi. Multi-objective based spectral unmixing for hyperspectral images," *ISPRS Journal of Photogrammetry and Remote Sensing*, vol. 124, pp. 54–69, 2017.

[28] J. M. Bioucas-Dias and M. A. Figueiredo, "Alternating direction algorithms for constrained sparse regression: Application to hyperspectral unmixing," *IEEE 2nd WHISPERS*, pp. 1–4, Jun. 2010.

[29] M. D. Iordache, J. Bioucas-Dias, and A. Plaza, "Total Variation Spatial Regularization for Sparse Hyperspectral Unmixing," *IEEE Trans. Geosci. Remote Sens.*, vol. 50, no. 11, pp. 4484 – 4502, Nov. 2012.

[30] Z. Shi, W. Tang, Z. Duren, and Z. Jiang, "Subspace matching pursuit for sparse unmixing of hyperspectral data," *IEEE Trans. Geosci. Remote Sens.*, vol. 52, no. 6, pp. 3256–3274, Jun. 2013.

[31] A. Halimi, P. Honeine, and J. Bioucas-Dias, "Hyperspectral Unmixing in Presence of Endmember Variability, Nonlinearity or Mismodelling Effects," *IEEE Trans. Image Process.*, vol. 25, no. 10, pp. 4565–4579, Oct. 2016.

[32] X. Fu, W.-K. Ma, J. Bioucas-Dias, and T.-H. Chan, "Semiblind hyperspectral unmixing in the presence of spectral library mismatches," *IEEE Trans. Geosci. Remote Sens.*, vol. 54, no. 9, pp. 5171–5184, Sep. 2016.

[33] P. A. Thouvenin, N. Dobigeon, and J. Y. Tourneret, "Online unmixing of multitemporal hyperspectral images accounting for spectral variability," *IEEE Trans. Image Process.*, vol. 25, no. 9, pp. 3979–3990, Sep, 2016.

[34] Bhatt, Jignesh S., Manjunath V. Joshi, and Mehul S. Raval. "A regularization based method for spectral unmixing of imaging spectrometer data." *SPIE Remote Sensing. International Society for Optics and Photonics*, vol. 85, no. 37, Nov. 2012.

[35] M. D. Dyar, M. E. Gunter, D. Tasa, *Mineralogy and Optical Mineralogy.* Chantilly, Virginia: Mineralogical Society of America, 2008.

[36] R. N. Clark, "Chapter 1: Spectroscopy of Rocks and Minerals, and Principles of Spectroscopy, in Manual of Remote Sensing", *Remote Sensing for the Earth Sciences.* New York: John Wiley and Sons, Vol. 3, pp. 3–58, 1999.

[37] J. Eckstein and D. Bertsekas, "On the Douglas-Rachford splitting method and the proximal point algorithm for maximal monotone operators," *Math. Program. Ser. A/B*, vol. 55, no. 3, pp. 293–318, Jun. 1992.

[38] M. V. Afonso, J. M. Bioucas-Dias, and M. A. Figueiredo, "An augmented lagrangian approach to the constrained optimization formulation of imaging inverse problems," *IEEE Trans. Image Process.*, vol. 20, no. 3, pp. 681–695, Mar. 2011.

[39] R. N. Clark, G. A. Swayze, R. Wise, E. Livo, T. Hoefen, R. Kokaly, and S. J. Sutley, *USGS digital spectral library splib06a.* US Geological Survey Denver, CO, 2007.

[40] A. F. Wells, *Structural Inorganic Chemistry, 5th edition.* New York: Oxford University Press, pp. 186, 1984.

[41] D. Marinova, V. Karadjova, D. Stoilova, "Infrared spectroscopic study of SO_4^{2-} ions included in $M_2'M''(SeO_4)_2 \cdot 6H_2O(M' = K, NH_4^+; M'' = Mg, Co, Ni, Cu, Zn)$ and NH_4^+ ions included in $K_2M(XO_4)_2 \cdot 6H_2O(X = S, Se; M = Mg, Co, Ni, Cu, Zn)$." *Spectrochim Acta A: Molecular and*

Biomolecular Spectroscopy, Vol. 134, pp. 526–534, Jan. 2013.

[42] G. R. Hunt, "Spectral signatures of particulate minerals in the visible and near infrared." *Geophysics*, Vol. 42, pp. 501–513, Apr. 1977.

[43] R. Burns, *Mineralogical Applications of Crystal Field Theory, Second Edition.* Cambridge: Cambridge University Press, pp. 551, 1993.

[44] V. C. Farmer, *The Infra-Red Spectra of Minerals.* London: Mineralogical Society, pp. 539, 1974.

[45] R. V. Morris, H. V. Lauer, C. A. Lawson, E. K. Gibson, G. A. Nace, and C. Stewart, "Spectral and other physiochemical properties of submicron powders of hematite ($-Fe_2O_3$), maghemite ($-Fe_2O_3$), maghemite ($-Fe_3O_4$), goethite ($-FeOOH$), and lepidochrosite ($-FeOOH$)", *J. Geophys. Res.* Vol. 90, pp. 3126–3144, Mar. 1985.

[46] G. Herzberg, *Molecular spectra and molecular structure, II, Infrared and Raman spectra of polyatomic molecules*, New York: Van Nostrand Reinhold, pp. 632, 1945.

[47] A. Bruckstein, M. Elad, and M. Zibulevsky, "On the uniqueness of nonnegative sparse solutions to underdetermined systems of equations," *IEEE Trans. Inf. Theory*, vol. 54, no. 11, pp. 4813–4820, Nov. 2008.

[48] K. E. Themelis, A. A. Rontogiannis, and K. D. Koutroumbas, "A novel hierarchical bayesian approach for sparse semisupervised hyperspectral unmixing," *IEEE Trans. Signal Process.*, vol. 60, no. 2, pp. 585–599, Feb. 2012.

[49] R. Tibshirani, "Regression shrinkage and selection via the lasso," *J. R. Statist. Soc. B*, vol. 58, no. 1, pp. 267–288, 1996.